7

Molecular Electron Microscopy Approaches to Elucidating the Mechanisms of Protein Fibrillogenesis

Hilal A. Lashuel and Joseph S. Wall

Summary

Electron microscopy (EM) has played a central role in our current understanding of the mechanisms underlying the pathogenesis of several amyloid diseases, including Alzheimer's disease, Parkinson's disease, and prion diseases. In this chapter, we discuss the application of various EM techniques to monitor and characterize quaternary structural changes during amyloid fibril formation in vitro and the potential of extending some of these techniques to characterizing ex vivo material. In particular, we would like to bring to the attention of the reader two very powerful molecular EM techniques that remain under utilized by researchers in the amyloid community, namely scanning transmission electron microscopy and single particle molecular averaging EM. An overview of the strength and limitations of these techniques as tools for elucidating the structural basis of amyloid fibril formation will be presented.

Key Words: Electron microscopy (EM); scanning transmission electron microscopy (STEM); single particle analysis; negative staining; α-synuclein, amyloid-β (Aβ); amyloid; fibrils; protofibrils; oligomers; sedimentation velocity analytical ultracentrifugation (SVAU).

1. Introduction

The extracellular and/or intracellular aggregation of a subset of proteins in the form of amyloid fibrils is a defining neuropathological hallmark that is shared by several clinically and pathologically distinct neurodegenerative and systemic diseases, including Alzheimer's disease (AD), Parkinson's disease (PD), Prion diseases, and systemic amyloidoses ***(1,2)***. The finding of these deposits in the vicinity of dying tissues and neurons suggested that they play a role in neurodegeneration and/or organ dysfunction. However, the first clues concerning the nature of these deposits became apparent only after the introduction of electron microscopy in the late 1950s ***(3–5)***. Electron microscopic examination of ex vivo amyloid fibrils composed of various proteins revealed long and

From: *Methods in Molecular Biology, vol. 299: Amyloid Proteins: Methods and Protocols*
Edited by: E. M. Sigurdsson © Humana Press Inc., Totowa, NJ

unbranching fibrils that are typically 10 nm in diameter. The possibility that soluble prefibrillar oligomeric species, rather than the fibrils, could be the pathogenic species in AD and related amyloid diseases arose as a result of the detection and characterization of prefibrillar β-sheet rich oligomeric species, termed protofibrils, during the fibrillization of Aβ and other amyloid forming proteins in vitro by electron microscopy (EM) and atomic force microscopy (AFM) ***(6–8)***. Later observations demonstrating that protofibrillar species alter neuronal function and/or cause cell death ***(9–12)*** have given rise to the hypothesis that protofibrils might be the primary pathogenic species in AD and related amyloid diseases ***(13,14)***. Therefore, in addition to playing a central role in defining the pathology of amyloid diseases, electron microscopy continues to be instrumental in providing key mechanistic insights into the role of amyloid fibril formation and the modes by which this process contributes to the pathogenesis of amyloid diseases, which are critical for developing effective therapeutic strategies to treat and/or prevent these devastating diseases.

The highly associated, non-crystalline, and insoluble nature of amyloid fibrils has precluded high-resolution structure determination by nuclear magnetic resonance (NMR) or X-ray crystallography. In addition, the morphological and size heterogeneity of fibril preparations and the absence of protocols for preparing and isolating stable intermediates along the amyloid pathway in monodisperese form remain major hurdles to understanding the structure and function of protofibrils and fibrils. The structures of amyloid fibrils derived from several proteins have therefore been studied by alternative structural approaches, including EM, AFM, and X-ray fiber diffraction ***(15,16)***.

The greatest advantage of EM over other structural techniques is that: (i) it does not require samples to be crystalline, (ii) it enables the study of transient quaternary structural intermediates, (iii) it requires a small amount of sample relative to NMR and X-ray crystallography, and (vi) there is no upper limit for the size of the molecule to be studied. Samples are usually preserved in a heavy metal stain (negative stain) or in a hydrated state at liquid nitrogen temperatures (CryoEM). Samples for scanning transmission electron microscopy (STEM) are usually freeze-dried to minimize biochemical alteration and permit quantitative microscopy. Recent advances in cryo electron microscopy and image processing techniques have enabled detailed structural studies of large macromolecular assemblies, including protofibrils and amyloid fibrils ***(17–25)***. In this chapter, we will present a brief summary of the application, strength, and limitations of some EM techniques that include negative staining electron microscopy, scanning transmission electron microscopy, and single particle averaging and image processing as tools for elucidating the structural basis of amyloid fibril formation.

1.1. Negative Staining Electron Microscopy

Negative staining EM is a simple technique that allows rapid and routine morphological and structural examination of biological macromolecules and macromolecular assemblies. Negative staining EM offers several distinct advantages over other techniques: 1) it is technically simple to perform; 2) it produces high contrast images; 3) it is relatively insensitive to damage to the specimen by the electron beam; 4) samples are easy to prepare (2–4 min) (*see* **Note 1**); and 5) it requires only a small amount of sample (2–5 μL). The procedure for negative stain EM involves adsorption onto a surface of a carbon coated formvar film that is attached to an EM grid followed by staining with heavy-metal solution and drying. Contrast is introduced by interaction of the electron beam with the sample regions having differing scattering power. Since macromolecules are composed mainly of atoms (e.g., C, H, O, N) that scatter electrons weakly, the EM images produced are of low contrast. Therefore, image contrast is maximized by embedding the sample in a thin layer of heavy metal stain such as uranyl acetate and uranyl formate (*see* **Note 2**). The thin shell of heavy metal atoms surrounding the sample scatters the electron beam more strongly than the sample itself, giving negative contrast. To improve the adsorption of particles to the grid, the surface of the carbon-coated EM grid is made more hydrophilic by glow discharging prior to use. Some of the problems encountered with negatively stained specimens are that: (i) the resolution is limited to about 25 Å, (ii) the structure is usually flattened owing to drying of the sample, (iii) different quaternary structures exhibit differential adsorption and/or orientation to the carbon coated grid, (iv) uneven staining could result in some image artifacts, and (v) the high ionic strength and non-physiological pH of the stain may alter the specimen.

Cryo-electron microscopy overcomes most of these limitations imposed by negative staining and has been used to achieve near atomic resolution in the most favorable cases. In cryo-EM, the samples are preserved in their hydrated state in ice by quick freezing in liquid nitrogen or ethane, and are imaged at low to moderate dose by EM to minimize damage to the sample (*see* review in ***[26]***).

1.2. Single Particle Analysis and Image Processing

In addition to negative staining EM, single particle averaging has recently emerged as a powerful technique in the structural studies of heterogeneous specimens such as those characterstic of protofibrils and fibril preparations of amyloidogenic proteins. **Figure 1** outlines the different steps involved in single particle averaging. Data collection: large sets of electron micrographs are collected and the appropriate images are then digitized for computational image processing. Particle selection: the first step involves manual selection of single

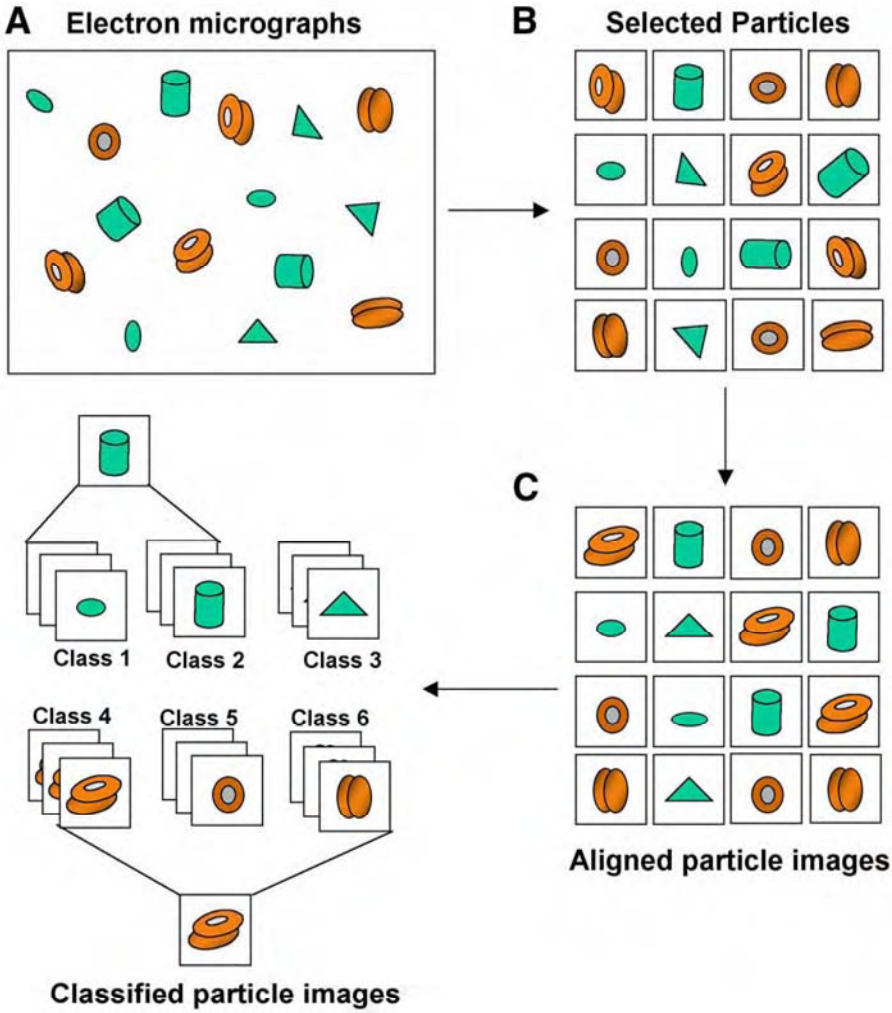

Fig. 1. Single particle analysis and image processing. **(A)** Cartoon depiction of sample micrograph showing different views of the objects under study. **(B)** Sixteen selected particle images from micrograph shown in **A**. **(C)** Aligned particle images. Each of the sixteen images now positioned to a common view. **(D)** Classified particle images. Sixteen unique views that were present in the original micrograph have resulted in six particle image classes. Classes 4, 5, and 6 represent three different views corresponding to the side, front, and top of the object.

projected electron microscopic particle images from the digitized electron micrographs. Since proteins adsorb on the carbon film in one or a few preferred orientations, the projected images may reflect many views of the protein. Particle

alignment: the particles are then centered, aligned with respect to each other, ordered, and subjected to computational classification using one of several commercial image processing programs (e.g., SPIDER image processing package *[27]*). Particle classification: involves an iterative process of several rounds of alignment and classification, in which the aligned images that project the same particle image, but differ in their orientation, i.e., the images are related to each other by a simple rotation in the plane of the image, are sorted into a specific number of output classes. The clustered raw images in each class are then averaged to yield average images for each class. Therefore computational classification is an excellent tool that allows single particle microscopy to work with heterogeneous samples. In cases where a monodisperse specimen can be prepared, the images making up the different classes can be used in 3D reconstruction for each class by random conical tilt approach. Although 3D reconstruction of negatively stained samples is limited to a resolution of 25Å, higher resolution (2–6 Å) structural details can be obtained using cryo EM and single-particle 3D image reconstruction techniques. In Cryo EM, the specimen is visualized in a native-like environment (hydrated), thus eliminating stain and drying artifacts. Furthermore, the structural integrity of the specimens is preserved by imaging at low electron dose. However, Cryo EM of heterogeneous specimens is complicated by low contrast, which makes it difficult to differentiate EM projections of identical particles displaying different orientations from those of different structures.

1.2.1. Characterization of Amyloid Fibrils by Single Particle Averaging of Embedded Sectioned Specimen

Single particle averaging provided the first detailed images of the fibril substructure demonstrating that amyloid fibrils are composed of several thin protofilaments which undergo lateral association and/or intertwine around each other to form the ribbon and cable-like morphologies characteristic of amyloid fibrils. Using single particle averaging of cross-section EM images of different mutant (V30M) transthyretin (TTR) amyloid fibrils from the vitreous humors of patients with familial amyloid polyneuropathy, Serpell et al. demonstrated that TTR fibrils are composed of four protofilaments organized around a electron-lucent central core, indicative of the presence of a hollow center, or central channel (**Fig. 2**) *(19)*. These observations have been confirmed by many subsequent studies. For example, recent cross sectional analysis studies of ex vivo amyloid fibrils composed of amyloidogenic proteins (Amyloid A protein, monoclonal immunoglobulin lambda light chain, Leu60Arg variant of apolipoprotein AI, and Asp67His variant lysozyme, and fibrils prepared from synthetic peptides [TTR 10–19] using single particle averaging *[28]*) revealed that amy-

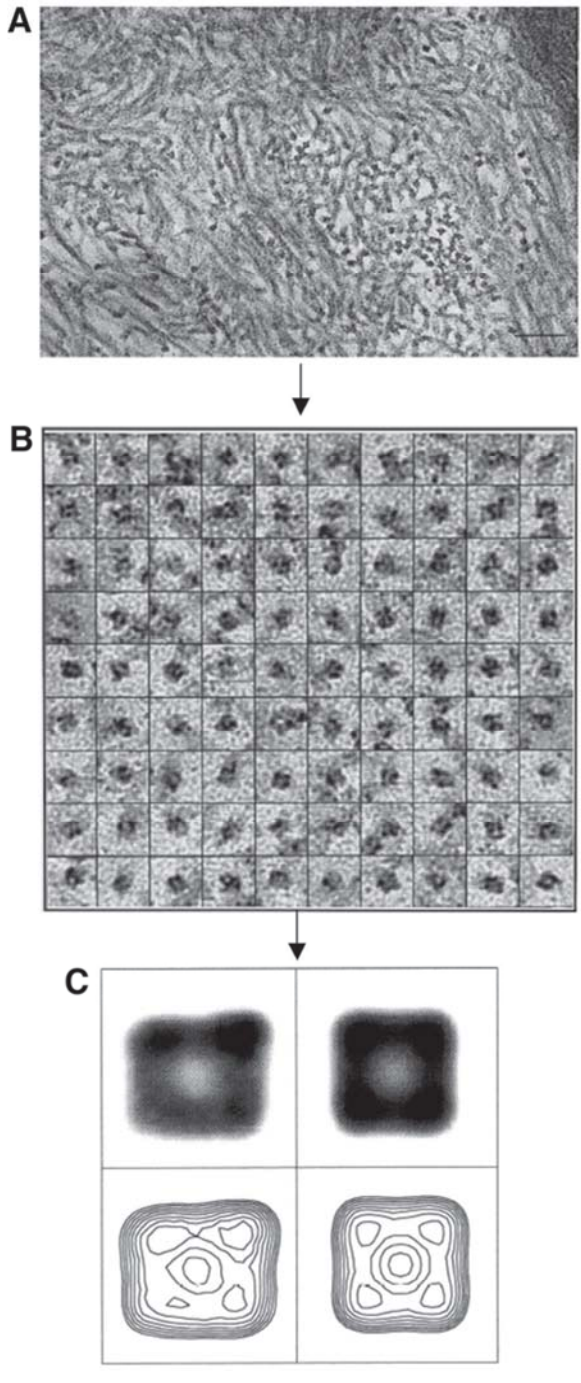
A
B
C

loid fibrils have an electron-lucent center around which the protofilaments making up the fibrils are organized.

1.2.2. Cryo Electron Microscopy and Single Particle 3D Image Reconstruction of Amyloid Fibrils

Recently, combining single particle averaging and cryo-EM methods has enabled 3D reconstruction of amyloid fibrils. This approach has been successful in providing a detailed structural view of the amyloid fibrils composed of SH3 domain of phosphatidylinositol-3'-kinase, revealing a double helix of two protofilament pairs intertwined around a hollow core, with a helical crossover repeat of approx 600 Å and an axial subunit repeat of approx 27 Å (**Fig. 3**) ***(20)***. Jimenez et al. (1999) divided the fibril images into individual crossover repeats (total of 890) and treated these as single particles. The cut-out repeats were iteratively aligned and classified by multivariate statistical analysis according to their length (**Fig. 3B**). 3D maps were then calculated from the individual classes using helical reconstruction, yielding a 3D reconstructed structure at 25 Å resolution (**Fig. 3B**). Since amyloid fibrils are long structures formed by repeated structural units, many fewer micrographs would be required for 3D reconstructions, in favorable cases.

1.2.3. Characterization of Protofibrils by Negative Stain EM and Single Particle Averaging

In collaboration with Dr. Thomas Walz and coworkers at Harvard Medical School, we have taken advantage of the capabilities of single particle electron microscopy to study heterogeneous protofibril samples of amyloid-β (Aβ) and α-synuclein. To gain further insight into the structural properties of α-synuclein protofibrils, we analyzed protofibrillar fractions of A30P and A53T by negative stain EM and single particle averaging ***(23,24)***. The A30P variant was observed to promote the formation of annular, pore-like protofibrils, whereas A53T promotes formation of annular and tubular protofibrillar structures (**Fig. 4**), suggesting that α-synuclein is capable of forming a pore-like protofibrillar structure. The ring-shaped protofibrils have a diameter of 11 ± 1 nm, and an inner core of 2 to 3 nm, whereas the tube-like protofibrils showed similar diameter

---

Fig. 2. (*Opposite page*) Single particle analysis provided first glimpses of the substructure of amyloid fibrils. **(A)** Electron micrograph of fibril cross-sections (Scale bar = 100 nm). **(B)** A total of 210 cross-section images were selected and used for averaging, only 100 cross-sections selected are shown. **(C)** Resulting averaged images of fibril cross-section revealing images of structure have a fourfold symmetry, suggesting that V30M-TTR fibril is composed of four protofilaments organized around an electron lucent center. Adapted with permission, from ***(19)***.

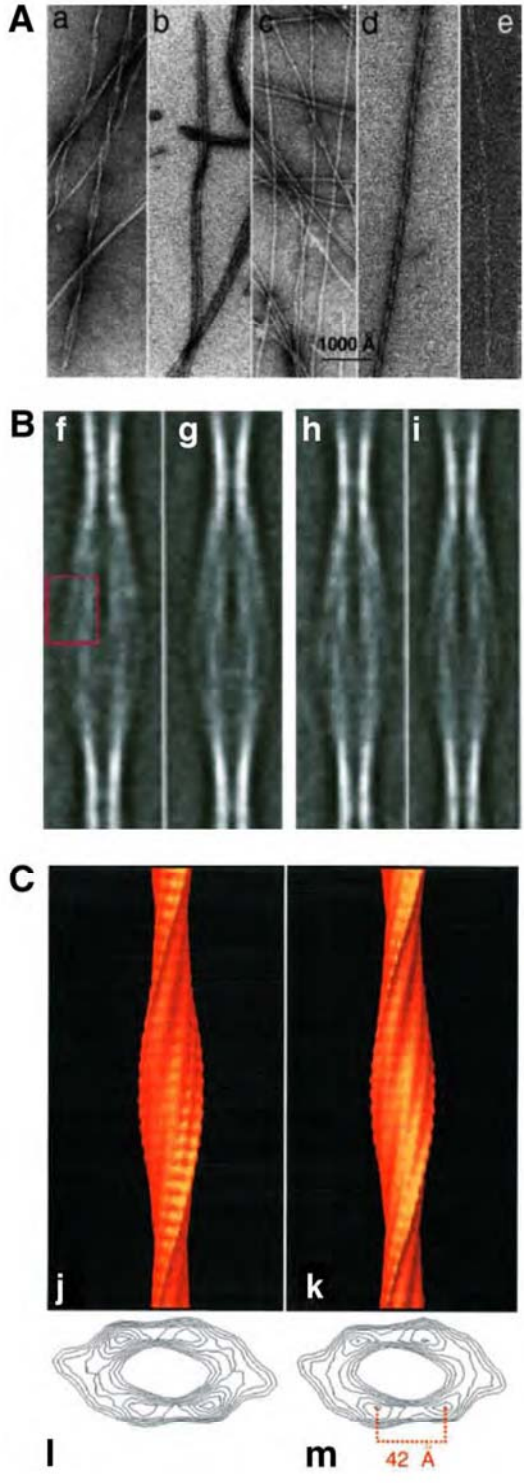
A
a
b
c
d
e
1000 Å
B
f
g
h
i
C
j
k
l
m
42 Å

(10–12 nm), but varied in length from 13 to 24 nm. The similar diameter observed for the annular and rectangular particles suggests that the two morphologies represent two different views (top and side view) of the same species. These results provided a possible structural basis for the pathogenic membrane permeabilization and channel activities reported for α-synuclein and Aβ ***(29–32)***. Further improvements in the preparation of highly homogeneous samples should enable higher resolution structural studies that would provide us with a powerful basis for understanding the mechanism of protofibril formation and assembly into fibrils, as well as the quaternary and tertiary structural changes required for protofibril interactions and/or insertion into membranes.

1.3. Scanning Transmission Electron Microscopy (STEM)

Several biophysical techniques (e.g., dynamic light scattering [DLS] and analytical ultracentrifugation [AU]) have been employed to monitor quaternary structural changes, which occur during amyloid fibril formation. In the case of heterogeneous samples, as is the case for amyloid forming proteins, AU and DLS provide average molecular masses that reflect the distribution of quaternary structures in solution. However, the morphological and size heterogeneity of the structures populated during protein fibrillogenesis precludes the assignment of MW averages to a particular quaternary structural species. STEM offers unique advantages over other mass determination techniques in its ability to image isolated and unstained biological molecules after freeze drying, allowing for accurate, quantitative dry mass determination of individual molecules as well as macromolecular assemblies (*see* **Note 3**). Furthermore, STEM requires only 2 to 5 µL of samples at concentrations ranging from 10 to 500 µg/mL (*see* **Note 4**), far less than what is required for AU and DLS experiments. The ability of STEM to provide accurate mass measurements of small quantities of heterogeneous samples provides it with an edge over other techniques when it comes to investigating the molecular mass and structural properties of

Fig. 3. (*Opposite page*) Cryo electron microscopy and single particle 3D image reconstruction of amyloid fibrils. **(A)** Negative-stain electron micrographs demonstrating the polymorphic nature of amyloid fibrils formed by SH3 domain of phosphatidylinositol-3'-kinase formed after several months of incubation at pH 2.0 (a–d). (e) The Cryo EM image of d. **(B)** The class averages of the 580 Å (f, 92 images) and 600 Å (h, 77 images) repeats used for reconstruction, reprojection of 3D reconstructions (g, i). The averages in B represent approx 19% of the entire data set. **(C)** 3D reconstructions and contoured density calculated from the 610 Å (j,l) and 580 Å (k,m) class averages reveal similar fibril structures composed of four protofilaments packed around a hollow core. In addition to the helical twist, the 27 Å subunit repeat is observable on the surface of the fibril structure and is more pronounced on the edge structures. (Adapted with permission, from **ref. *20***.)

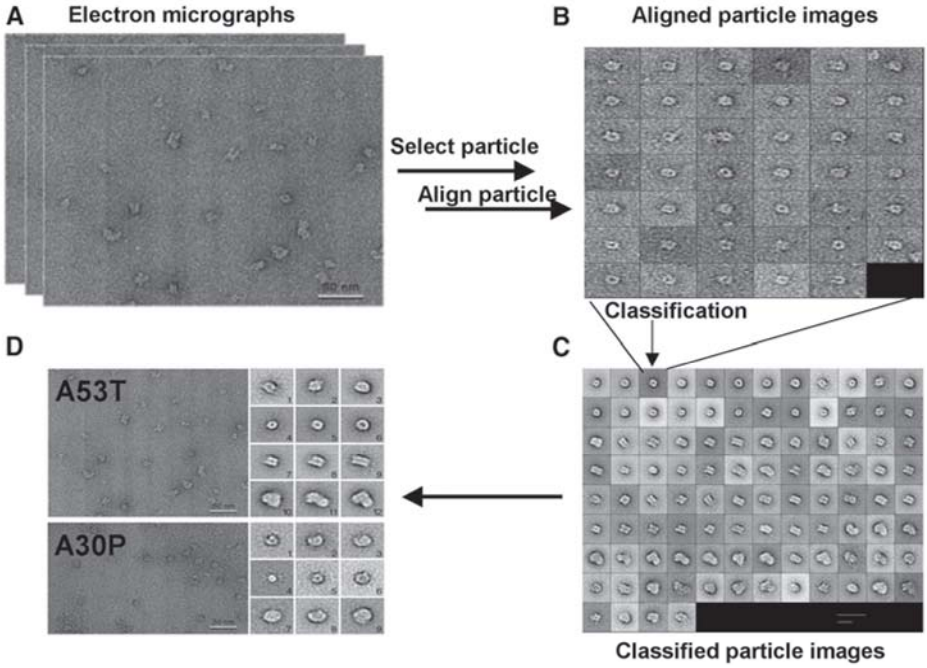

Fig. 4. Single particle averaging of A30P and A53T α-synuclein reveals a collection of distinct, yet related, protofibrillar species. **(A)** Representative images of negatively stained samples of A53T and A30P. For image processing, 31 images of A53T and 16 images of A30P were digitized with a Zeiss SCAI scanner using a pixel size of 4.04 Å at the specimen level. From the digitized images, 5815 (A53T), and 5040 (A30P) particles were selected for further computational processing using the SPIDER image processing package 39. The 5000 to 6000 particle images were subjected to ten rounds of alignment **(B)** and classification specifying 100 output classes **(C)**. These 100 classes fell into four major groups of structures. A gallery with representative class averages obtained from images of A53T and A30P are shown in **(D)**, illustrating the four major groups of protofibril structures. (Adapted from EM images provided by Dr. Thomas Walz and Benjamine Peter and reproduced with permission from **ref. *23***.)

biological samples isolated and purified from human tissues or cellular extracts. Therefore, STEM is an excellent tool for investigating the molecular mass and structural properties of transient quaternary structure intermediates during amyloid formation pathway in vitro or quaternary structures isolated from ex vivo material. Indeed, STEM has proven to be instrumental for investigating the mechanism of self-assembly and amyloid fibril formation of several proteins, including tau ***(33,34)***, Aβ ***(22,35–37)***, α-synuclein ***(23)***, transthyretin ***(38)***, and the Ure2p prion protein ***(39)***. The ability to monitor changes in mor-

phology and molecular mass during protein fibrillogenesis should bring us one step closer to understanding the structure of the various assembly intermediates on the pathway to amyloid formation and their structural relationship to the final product, the amyloid fibrils.

The STEM produces an image one point at a time by probing the sample with a focused electron beam and counting the emerging electrons on an array of detectors according to how much they are deflected in striking nuclei of atoms in the specimen. The image is formed by scanning the beam over the specimen in a TV-type raster while simultaneously recording the various detector signals, any one of which can be used to give an image. The detector measuring large-angle scattering gives a signal proportional to the mass of atoms in the path of the beam (heavy atoms scatter more strongly in proportion to their mass and interference effects between nearby atoms are minimal). We record the ratio of large angle scattering to total signal for all emerging electrons, so the measured scattering percentage is independent of incident beam current. Therefore the STEM image is essentially a map of the mass in each small element (pixel) of the image.

Ultimate spatial resolution is determined by the probe size, 0.25 nm for BNL STEM1 operating at 40 keV. Practical resolution is determined by radiation damage during imaging and any distortion owing to freeze-drying. STEM1 maintains the specimen at −150°C to minimize damage and detects every electron passing through the specimen so that no information will be wasted.

Mass measurement is performed offline using custom software, PCMass, which runs on a PC running Windows 95 or later. The program is available on the STEM FTP site (ftp.stem.bnl.gov) and provides image viewing, manual mass measurement, automated mass measurement, statistical summaries, and documentation.

The mass measurement procedure involves selecting isolated particles with a circle or rectangle. The program sums pixels within the marked area, computing the total mass of particle and underlying substrate. It then subtracts background on the assumption that the substrate under the particle has the same mass per unit area as that observed in "clean" areas between particles. Absolute accuracy ranges from roughly 10% for 100 kDa particles, to 4% for 1 MDa, and 2% for particles above 5 MDa. The useful range for compact particles is 30 kDa to over 1000 MDa. If the particle is extended in shape, more background is included and must be subtracted, giving slightly larger errors.

The mass calibration of the STEM is checked using tobacco mosaic virus (TMV) included in every freeze dry. This virus is easily distinguishable from most specimens being a rod 300 nm long and 18 nm in diameter with one concave end and one convex end. If the shape of the TMV is not that expected or if the mass per unit length is not 131 kDa/nm, the quality of the included specimen

is suspect and additional controls are required. Problems may arise owing to impurities in the specimen or buffers.

STEM measures both mass and length, so it is particularly suitable for studying filaments, giving mass per unit length. Furthermore, the distance of every pixel from the centerline of a filament or center of a particle is known accurately, giving a radial mass profile. If the object has spherical or cylindrical symmetry, the mass profile can be transformed to give a radial density profile.

The STEM mass measurements are most useful for characterizing the uniformity of a preparation, comparing native vs reconstituted structures and locating heavy atom labels. Since the STEM image is a projection with somewhat limited resolution, it does not give direct 3D models. However it is very powerful in distinguishing between several proposed models. An example is the work summarized in **Fig. 5**, which showed the organizing principle of prion filaments, namely that there is one subunit every 0.45 nm, the spacing of a β helix. The filaments have a central core surrounded by head groups whose size can be controlled by genetic manipulation.

STEM has also proven to be excellent tool for characterizing the homogeneity/heterogeneity as well as structural properties of transient quaternary structure intermediates "protofibrils" on the amyloid fibril formation pathway of several amyloid forming proteins, including Aβ ***(22,35–37)***, α-synuclein ***(23)***, and transthyretin ***(38)***. Recently, we employed STEM to characterize the molecular mass distribution of protofibrils and to estimate the stoichiometric composition of the various α-synuclein and Aβ protofibrillar structures (**Fig. 6**) ***(22,23)***. Quantitative STEM analysis of α-synuclein particles reveals a mass distribution consistent with that predicted by sedimentation velocity analytical ultracentrifugation (SVAU).

The STEM can image specimens in negative stain, but the added material makes mass measurements difficult to interpret. However, image contrast in the STEM can be enhanced electronically, making it possible to use negative stains with lower contrast as long as their signal to noise ratio is high. One such stain is methylamine vanadate ***(40)***, which is less grainy than uranyl salts and stable at pH 7.0. An example of prion filaments prepared with this stain is shown in **Fig. 7**. With its lower contrast, methylamine vanadate does not obscure heavy atom labels, which can be used to mark specific sites.

Fig. 5. (*Opposite page*) STEM mass analysis of filaments of Ure2p constructs. The upper panel shows dark-field micrographs. Type A (single) and Type B (paired) filaments are indicated. Bar = 100 nm. Left: Mass per unit length measurements for several constructs. Right: Average mass per unit length plotted against subunit mass for type A (full circles) and type B (open circles) filaments. Solid line is mass per unit length expected for one subunit every 4.5 nm. Adapted with permission from ***(39)***.

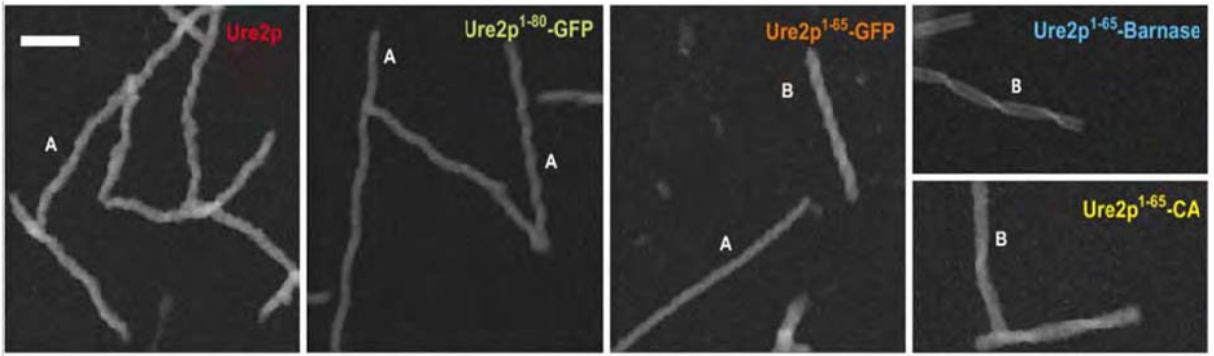
Ure2p
A
Ure2p1-80-GFP
A
A
Ure2p1-65-GFP
B
A
Ure2p1-65-Barnase
B
Ure2p1-65-CA
B

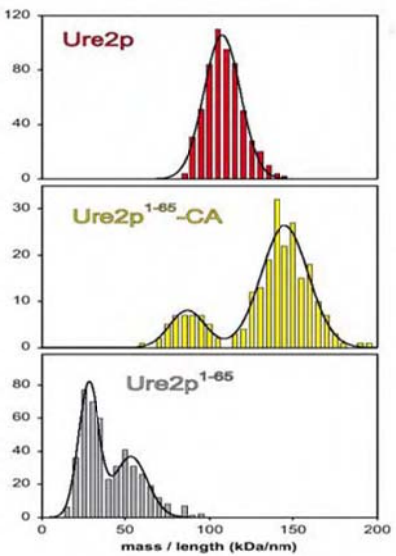
Ure2p
Ure2p1-65-CA
Ure2p1-65
mass / length (kDa/nm)

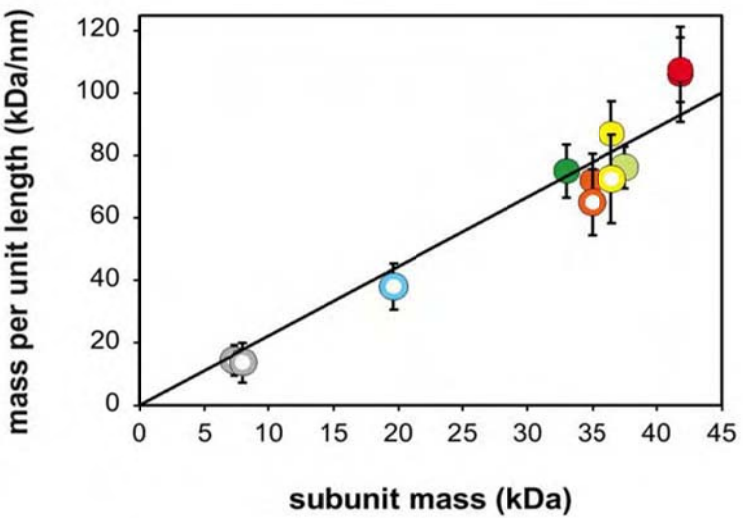
mass per unit length (kDa/nm)
subunit mass (kDa)

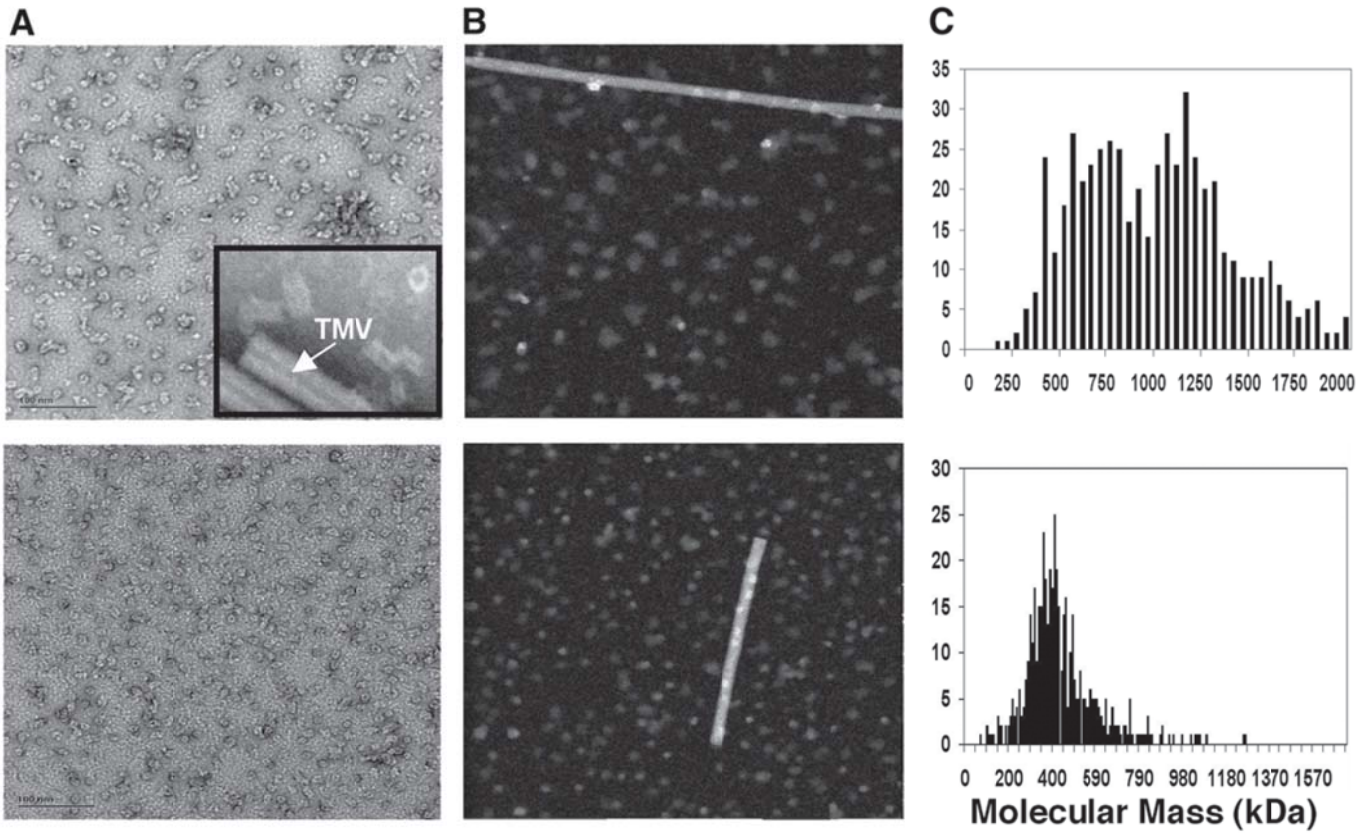
A
B
C
TMV
35
30
25
20
15
10
5
0
0 250 500 750 1000 1250 1500 1750 2000
30
25
20
15
10
5
0
0 200 400 590 790 980 1180 1370 1570
Molecular Mass (kDa)

2. Materials

1. Formvar carbon coated cooper grids (Electron Microscopy Sciences no. FCF200-Cu).
2. Carbon coated titanium grids for use in the STEM are prepared by the STEM staff.
3. EMS blocking solution (Electron Microscopy Sciences no. 25595).
4. Uranyl acetate (Electron Microscopy Sciences no. 22400).
5. Uranyl format (Pfaltz Bauer Inc. no. 06708).
6. Methylamine vanadate (NanoVan, NanoProbes, Inc. no. 2011).
7. Numbered grid storage box (Electron Microscopy Sciences no. 71138).
8. Buffer A: 5 m*M* Tris-HCl, 70 m*M* NaCl, pH 7.4.

3. Methods

3.1. Negative Staining Electron Microscopy

3.1.1. Preparing Uranyl Formate Solution for Negative Staining (0.6% [w/v])

1. Prepare a solution of 6 mg/mL of uranyl acetate in water.
2. Filter the solution through a 0.2-μm filter. The uranyl formate solution is ready to use.

3.1.2. Preparing Uranyl Formate Solution for Negative Staining (0.7% [w/v])

1. Weigh 37.5 mg of uranyl formate in a beaker and cover it to prevent exposure to light.
2. Bring 5 mL of H_2O to boil in a test tube (4.5–4.7 mL).
3. Add the boiling water to the uranyl formate in the beaker. Stir for 5 min.
4. Add 5 mL of NaOH (5 *M*) (a color change to a darker yellow should occur) (6–7 mL).
5. Stir for additional 5 min.
6. Filter through a 0.2-μm filter. The uranyl formate solution is ready to use.

Fig. 6. (*Opposite page*) Quantitative STEM analysis of two α-synuclein protofibril fractions separated by size exclusion chromatography reveals clear separation and mass distributions consistent with that predicted by SVAU. **(A)** Negatively stained (uranyl formate) electron micrographs of the two A53T α-synuclein protofibril fractions. **(B)** Electron micrograph of unstained/freeze-dried A53T-synuclein particles recorded by STEM. Light regions represent areas of high-mass density and dark regions represent areas of low mass density. **(C)** Histograms of molecular mass measurements of A53T protofibril fractions shown in (A). The inset in (A) shows an STEM micrograph of vanadate stained protofibrillar fraction of A53T revealing annular and tubular structures, similar to those seen in uranyl formate stained samples (**Fig. 4**).

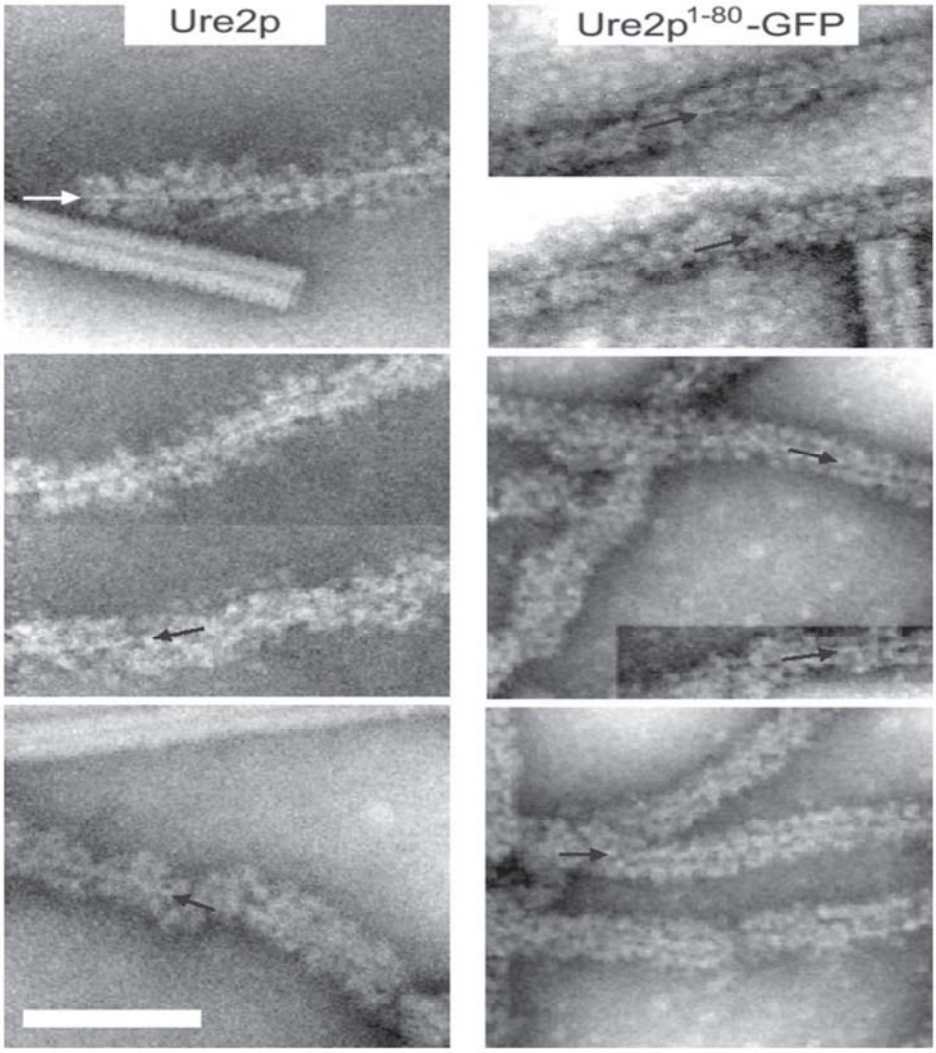

Fig. 7. Filaments of Ure2p visualized by dark-field STEM of vanadate stained specimens. Bar = 50 nm. Arrows indicate regions where the core fiber is clearly visualized. Adapted with permission from ***(39)***.

3.1.3. Staining Samples on Formvar-Carbon Coated Grids

1. Place a drop of the diluted material on a formvar and carbon-coated cooper grid.
2. After 30 to 60 s, blot off the excess liquid with filter paper.
3. Add a drop of uranyl acetate or uranyl formate solution.
4. After 1 min, blot off the excess with filter paper.

5. Allow the grid to air dry or apply a vacuum line to the edge of the grid.
6. Examine in the transmission electron microscope.

3.2. STEM Sample Preparation (Wet Film, Hanging Drop Method)

Specimens for the STEM are prepared by the STEM staff (*see* **Note 5**), but the details will be discussed here to enable the users to identify potential problems before sending samples for analysis to the STEM facility. When possible, it is recommended that samples should be screened in a conventional microscope under conditions used to prepare the sample for examination by the STEM (*see* **Note 6**).

1. The thin (2–3 nm) carbon film, which has been shadowed onto freshly cleaved rock salt, is floated off the crystal onto a dish of STEM water.
2. The titanium grids, covered with holey film (and for the STEM, in rings and caps), are placed face down on the floating carbon for approx 1 h.
3. A grid is picked up from above and retains a hanging droplet of water. It is washed and wicked with STEM water two or three times, never being allowed to dry. Water is applied from one side with an Eppendorf pipette and wicked from the other side with filter paper.
4. Three microliters of TMV at 100 μg/mL is injected into a drop and allowed to adsorb to the thin carbon film for 1 min.
5. The grid is then washed and wicked two or three times with injection buffer for the sample. Three microliters of the specimen is injected into the drop and allowed to adsorb for 1 min.
6. The grid is washed with sample buffer a couple of times, followed by washes (approx 10), ending with washes of 20 to 50 m*M* ammonium acetate. The intermediate washes depend on the sample buffer (e.g., high-salt buffers require washes with ammonium acetate).
7. For freeze-drying: after the final wash, the grid is briefly blotted between the two pieces of the filter paper, leaving a layer of liquid a few micrometers thick and rapidly plunged into liquid nitrogen slush to freeze it. (At this point, the grids may be stored under liquid nitrogen until STEM time is available for observation.) For negative staining: the last two washes are performed with a solution of 1% methylamine vanadate (NanoVan, NanoProbes, Inc.), then the grid is wicked as above and air dried.
8. For freeze drying: six samples are transferred from liquid nitrogen to slots in the precooled STEM freeze dry cartridge, freeze dried overnight under ultra-high vacuum, and transferred under vacuum to the STEM.

3.2.1. STEM Operation

To assure optimum data quality and efficient use of microscope time, a trained operator usually runs the STEM. Frequent users can obtain training on request, but the alacrity of most STEM experiments makes this unnecessary.

For a detailed description of how the STEM is operated *see* http://www.biology.bnl.gov/stem/stem.htm.

3.2.2. STEM Data Analysis

The STEM images are stored on a CD or hard drive and can be viewed using commercial software or PCMass mass-analysis program provided by the STEM group. The format of the Brookhaven National Laboratory (BNL) STEM images is a header 4096 bytes long, followed by two 512 × 512, 8-bit images interleaved. Adobe Photoshop can import these images in the "RAW" mode for contrast adjustment, annotation, and publication.

4. Notes

1. Most commonly used buffers (Tris-HCl, HEPES, and MOPS) are amenable to preparation of stained or frozen samples. Additives such as sucrose, glycerol, or dithiothreitol will usually wash off. Phosphate buffers often do not wash off well and leave bright spots, which interfere with STEM analyses.
2. The choice of heavy metal stain will depend on the stability of the specimen at the pH of the staining solution. Uranyl acetate and uranyl formate (0.5–2.0%) have a low pH (pH 4.2–4.5) and would not be recommended for samples that are unstable at these pHs. Neutral phosphotungstic acid is a useful stain for such samples, but produces less contrast than uranyl acetate. A 1% to 3% solution of phosphotungstic acid is made up in water and the pH is adjusted to 7.0 using sodium hydroxide with 1 N NaOH. When working with a new sample, it is recommended to try at least two different stains with different staining properties (e.g., uranyl acetate, phosphotungstic acid, vandate). Alternatively, macromolecular assemblies can be stabilized against pH-induced dissociation by brief exposure (approx 15 min) to general fixative and crosslinking reagents such as gluteraldehyde and formaldehyde (approx 0.1%) before applying them to the grid.
3. The expected mass accuracy depends on particle size, shape, and measuring dose. A 100 kDa globular particle on a 2-nm carbon substrate measured with a dose of 10 $\mu l/A^2$ should give a standard deviation (SD) of 10%, whereas a 1-MDa particle should give 2%. If the particle is extended or the background is dirty, the SD will be worse. The TMV reference particles should give mass per unit length of 13.1 kDa/A with a SD of 1%. When possible, it is critical to compare mass measurements from STEM to those determined by AU and/or DLS to eliminate the possibility that mass estimates by STEM might be biased towards a particular quaternary structure owing to differential adsorption to the EM grid.
4. Only small concentrations of samples are needed for examination in the STEM, but it is useful if the concentration is relatively high. Ideally 10 to 50 µL of sample at 100 to 200 µg/mL is adequate, from which a series of dilutions will be prepared and examined.
5. The STEM is a NIH Research Resource. As such, it is available to users with appropriate projects free of charge. A project is usually initiated by a discussion

of it on the phone or by e-mail. A trial sample is sent by overnight mail to BNL. The grids are prepared on the day the samples arrive, if it has been prearranged. The grids are stored in a grid fridge under liquid nitrogen (stable for years) until they can be freeze-dried and examined in the microscope. Additional details about the facility can be found on http://www.biology.bnl.gov/stem/stem.html. Additional support is provided by the United States Department of Energy.

6. All samples for STEM must be physically clean. Any contamination from the purification procedures, such as column or gel material, or other physical additives that scatter electrons will interfere with the observation and analysis. Detergent should be avoided if at all possible.

Acknowledgments

We would like to thank Dr. Thomas Walz, Benjamin Petre, Dr. Louise Serpell, Dr. Helen Saibil, and Dr. Alasdair C. Steven for permitting reproduction of their data in this chapter. The molecular EM facility at Harvard Medical School was established by a generous donation from the Giovanni Armenise Harvard Center for Structural Biology and is maintained by funds from NIH grant GM62580. The Brookhaven National Laboratory STEM is an NIH Supported Resource Center, NIH P41-EB2181, with additional support provided by the Department of Energy (DOE) and the Office of biological and environmental research (OBER). Support was also derived from a sabbatical fellowship (H.A.L) from the Harvard Center for Neurodegeneration and Repair and NIH (AG08470).

References

1 Selkoe, D. J. (2003) Folding proteins in fatal ways. *Nature* **426(6968),** 900–904.
2 Rochet, J. C. and Lansbury, P. T. Jr. (2000) Amyloid fibrillogenesis: themes and variations. *Curr. Opin. Struct. Biol.* **10(1),** 60–68.
3 Paul, W. E. and Cohen, A. S. (1963) Electron microscopic studies of amyloid fibrils with ferritinconjugated antibody. *Am. J. Pathol.* **43,** 721–738.
4 Cohen, A. S. (1965) The constitution and genesis of amyloid. *Int. Rev. Exp. Pathol.* **4,** 159–243.
5 Bladen, H. A., Nylen, M. U., and Glenner, G. G. (1966) The ultrastructure of human amyloid as revealed by the negative staining technique. *J. Ultrastruct. Res.* **14(5),** 449–459.
6 Harper, J. D., Lieber, C. M., and Lansbury, P. T. Jr. (1997) Atomic force microscopic imaging of seeded fibril formation and fibril branching by the Alzheimer's disease amyloid-beta protein. *Chem. Biol.* **4(12),** 951–959.
7 Harper, J. D., et al. (1997) Observation of metastable Abeta amyloid protofibrils by atomic force microscopy. *Chem. Biol.* **4(2),** 119–125.
8 Walsh, D. M., et al. (1997) Amyloid beta-protein fibrillogenesis. Detection of a protofibrillar intermediate. *J. Biol. Chem.* **272(35),** 22364–22372.

9 Lambert, M. P., et al. (1998) Diffusible, nonfibrillar ligands derived from Abeta1-42 are potent central nervous system neurotoxins. *Proc. Natl. Acad. Sci. USA* **95 (11),** 6448–6453.
10 Hartley, D. M., et al. (1999) Protofibrillar intermediates of amyloid beta-protein induce acute electrophysiological changes and progressive neurotoxicity in cortical neurons. *J. Neurosci.* **19(20),** 8876–8884.
11 Walsh, D. M., et al. (2002) Naturally secreted oligomers of amyloid beta protein potently inhibit hippocampal long-term potentiation in vivo. *Nature* **416(6880),** 535–539.
12 Bucciantini, M., et al. (2002) Inherent toxicity of aggregates implies a common mechanism for protein misfolding diseases. *Nature* **416(6880),** 507–511.
13 Goldberg, M. S. and Lansbury, P. T. Jr. (2000) Is there a cause-and-effect relationship between alpha-synuclein fibrillization and Parkinson's disease? *Nat. Cell Biol.* **2(7),** E115–E119.
14 Caughey, B. and Lansbury, P. (2003) Protofibrils, pores, fibrils, and neurodegeneration: separating the responsible protein aggregates from their innocent bystandards. *Annu. Rev. Neurosci.* **26,** 267–298.
15 Serpell, L. C., Fraser, P. E., and Sunde, M. (1999) X-ray fiber diffraction of amyloid fibrils. *Methods Enzymol.* **309,** 526–536.
16 Serpell, L. C. (2000) Alzheimer's amyloid fibrils: structure and assembly. *Biochim. Biophys. Acta* **1502(1),** 16–30.
17 Saibil, H. R. (2000) Macromolecular structure determination by cryo-electron microscopy. *Acta Crystallogr. D Biol. Crystallogr.* **56(Pt 10),** 1215–1222.
18 Radermacher, M., et al. (1987) Three-dimensional reconstruction from a single-exposure, random conical tilt series applied to the 50S ribosomal subunit of Escherichia coli. *J. Microsc.* **146(Pt 2),** 113–136.
19 Serpell, L. C., et al. (1995) Examination of the structure of the transthyretin amyloid fibril by image reconstruction from electron micrographs. *J. Mol. Biol.* **254(2),** 113–118.
20 Jimenez, J. L., et al. (1999) Cryo-electron microscopy structure of an SH3 amyloid fibril and model of the molecular packing. *Embo J.* **18(4),** 815–821.
21 Jimenez, J. L., et al. (2002) The protofilament structure of insulin amyloid fibrils. *Proc. Natl. Acad. Sci. USA* **99(14),** 9196–9201.
22 Lashuel, H., et al. (2003) Mixtures of wild-type and "Arctic" Abeta40 in vitro accumulate protofibrils, including amyloid pores. *J. Mol. Biol.* **332(4),** 795–808.
23 Lashuel, H., et al. (2002) alpha-Synuclein, especially the Parkinson's disease-associated mutants, forms pore-like annular and tubular protofibrils. *J. Mol. Biol.* **322(5),** 1089.
24 Lashuel, H. A., et al. (2002) Neurodegenerative disease: amyloid pores from pathogenic mutations. *Nature* **418(6895),** 291.
25 Wang, L., et al. (2002) Murine apolipoprotein serum amyloid A in solution forms a hexamer containing a central channel. *Proc. Natl. Acad. Sci. USA* **99(25),** 15947–15952.

26 Makin, O. S. and Serpell, L. C. (2002) Examining the structure of the mature amyloid fibril. *Biochem. Soc. Trans.* **30(4),** 521–525.

27 Frank, J., et al. (1996) SPIDER and WEB: processing and visualization of images in 3D electron microscopy and related fields. *J. Struct. Biol.* **116(1),** 190–199.

28 Serpell, L. C., et al. (2000) The protofilament substructure of amyloid fibrils. *J. Mol. Biol.* **300(5),** 1033–1039.

29 Volles, M. J., et al. (2001) Vesicle permeabilization by protofibrillar alpha-synuclein: implications for the pathogenesis and treatment of Parkinson's disease. *Biochemistry* **40(26),** 7812–7819.

30 Volles, M. J. and Lansbury, P. T. Jr. (2002) Vesicle permeabilization by protofibrillar alpha-synuclein is sensitive to Parkinson's disease-linked mutations and occurs by a pore-like mechanism. *Biochemistry* **41(14),** 4595–4602.

31 Kagan, B. L., et al. (2002) The channel hypothesis of Alzheimer's disease: current status. *Peptides* **23(7),** 1311–1315.

32 Kourie, J. I., et al. (2002) Heterogeneous amyloid-formed ion channels as a common cytotoxic mechanism: implications for therapeutic strategies against amyloidosis. *Cell. Biochem. Biophys.* **36(2-3),** 191–207.

33 King, M. E., et al. (2001) Structural analysis of Pick's disease-derived and in vitro-assembled tau filaments. *Am. J. Pathol.* **158(4),** 1481–1490.

34 Ksiezak-Reding, H., et al. (1996) Ultrastructural instability of paired helical filaments from corticobasal degeneration as examined by scanning transmission electron microscopy. *Am. J. Pathol.* **149(2),** 639–651.

35 Antzutkin, O. N., et al. (2002) Supramolecular structural constraints on Alzheimer's beta-amyloid fibrils from electron microscopy and solid-state nuclear magnetic resonance. *Biochemistry* **41(51),** 15436–15450.

36 Antzutkin, O. N. (2004) Amyloidosis of Alzheimer's Abeta peptides: solid-state nuclear magnetic resonance, electron paramagnetic resonance, transmission electron microscopy, scanning transmission electron microscopy and atomic force microscopy studies. *Magn. Reson. Chem.* **42(2),** 231–246.

37 Goldsbury, C. S., et al. (2000) Studies on the in vitro assembly of a beta 1-40: implications for the search for a beta fibril formation inhibitors. *J. Struct. Biol.* **130(2-3),** 217–231.

38 Cardoso, I., et al. (2002) Transthyretin fibrillogenesis entails the assembly of monomers: a molecular model for in vitro assembled transthyretin amyloid-like fibrils. *J. Mol. Biol.* **317(5),** 683–695.

39 Baxa, U., et al. (2003) Architecture of Ure2p prion filaments: the N-terminal domains form a central core fiber. *J. Biol. Chem.* **278(44),** 43717–43727.

40. Tracz, E., et al. (1997) Paired helical filaments in corticobasal degeneration: the fine fibrillary structure with NanoVan. *Brain Res.* **773(1-2),** 33–44.